Dalton Transactions

ROYAL SOCIETY OF CHEMISTRY

PAPER

View Article Online
View Journal | View Issue

Cite this: *Dalton Trans.*, 2025, **54**, 9901

Nb(v), Ta(v), and V(iv) catalyst-driven development of temperature-responsive self-healing materials based on methyl methacrylate†

Joanna Drzeżdżon, *[a,b] Marzena Białek, [c] Stefania Zappia,[d] Mattia Lopresti,[e] Luca Palin,[e,f] Katarzyna N. Jarzembska, [g] Radosław Kamiński [g] and Janusz Datta [b]

This study fills an important gap in the use of group V cation complexes – Nb(v), Ta(v), V(iv) – as versatile catalysts that can be used both in the polymerisation of olefins and in the synthesis of MMA-based materials that exhibit temperature-responsive properties and self-healing capabilities. This area has so far remained insufficiently explored. The work shows clear structure–property relationships of the materials and highlights their potential for green applications. This work introduces newly developed crystalline coordination compounds of Nb(v), Ta(v), and V(iv), synthesized with ligands such as 2-phenylpyridine, 4-phenylpyridine, and dimethylformamide (DMF). These complexes were explored as catalysts in both ethylene polymerization and its copolymerization with 1-octene, in addition to their role in forming temperature-responsive, self-healing materials based on methyl methacrylate (MMA). The catalysts demonstrated notable versatility, effectively enabling the synthesis of traditional polyolefins as well as advanced MMA-derived polymers with adaptive features. Rheological and mechanical testing showed that both the choice of catalyst and the concentration of MMA significantly impacted key material properties, including viscosity, shear stress, hardness, and healing capability. Particularly impressive were the V(iv)-based catalysts, which enabled rapid self-healing. For instance, the V-PE-50MMA composition achieved full structural recovery within just 15 minutes at 35 °C. Microscopic analysis revealed a transformation in material structure—from dense to porous forms—as MMA content increased, which was linked to stronger molecular interactions.

Received 7th May 2025,
Accepted 29th May 2025

DOI: 10.1039/d5dt01073j

rsc.li/dalton

1. Introduction

The development of self-healing materials inspired by biological processes has become the subject of considerable interest as a sustainable approach to increasing product durability and reducing resource consumption.[1] In nature, biological systems have remarkable self-healing mechanisms that allow organisms to recover from damage through molecular reorganization and regenerative processes. Applying these biological principles in the context of synthetic materials opens up new opportunities toward developing more durable and resource-efficient solutions, especially in the construction industry.[2,3] The most widely studied self-repairing materials are elastomers.[4,5] They have the ability to deform reversibly. Elastomers such as polyurethanes, silicone polymers and polybutadienes are widely studied for self-repair due to their ability to regenerate damaged bonds.[5]

Self-healing polymers represent a transformative development in materials science, providing the extraordinary capability for materials to autonomously repair damage without

[a]*Department of Environmental Technology, Faculty of Chemistry, University of Gdańsk, Wita Stwosza 63, 80-308 Gdańsk, Poland. E-mail: joanna.drzezdzon@ug.edu.pl*
[b]*Department of Polymer Technology, Gdańsk University of Technology, Narutowicza 11/12, 80-233 Gdańsk, Poland*
[c]*Department of Chemical Technology and Polymer Chemistry, Institute of Chemistry, University of Opole, Oleska 48, 45-052 Opole, Poland*
[d]*Istituto di Scienze e Tecnologie Chimiche "Giulio Natta" (SCITEC) of the Consiglio Nazionale delle Ricerche (National Research Council – CNR), via Alfonso Corti 12, 20133 Milano, Italy*
[e]*Department of Science and Technological Innovation, University of Eastern Piedmont, Viale T. Michel 11, 15121 Alessandria, Italy*
[f]*Nova Res s.r.l., Via D. Bello 3, 28100 Novara, Italy*
[g]*Faculty of Chemistry, University of Warsaw, Żwirki i Wigury 101, 02-089 Warsaw, Poland*

†Electronic supplementary information (ESI) available: All experimental part and an additional file contains test results for XRD, MALDI-TOF-MS, GPC, NMR, TG, DSC, FT-IR, physico-chemical analysis of complex compounds including elemental analysis. CCDC 2391112, 2391113 and 2383525. For ESI and crystallographic data in CIF or other electronic format see DOI: **https://doi.org/10.1039/d5dt01073j**

the need for external assistance. These polymers hold great promise, particularly for applications in environments where repair or maintenance is either difficult or expensive.[6] At present, the majority of research on self-healing polymers is focused on thermosetting polymers and those created through metathesis reactions.[7,8] Such processes often use noble metal catalysts, like ruthenium complexes. While these catalysts are highly effective, they are limited by high costs, scarce availability, and environmental concerns.[9,10] Table 1 presents examples of self-healing polymers along with their properties.

A recent study examined the use of poly(methyl methacrylate) (PMMA) capsules to introduce self-healing properties in concrete.[11] Their strength during the mixing process and their ability to react when cracks occur were studied. The results suggested that PMMA capsules with specific dimensions could be a promising solution for large-scale applications. In addition, studies have been conducted on core–shell nanocapsules, made of MMA and *N*,*N*-dimethylaniline, which act as a self-repairing agent for cementitious materials.[12] The results showed that the aforementioned nanocapsules, embedded in PMMA, release healing substances in response to the onset of stress. Other studies have used PMMA in organic–inorganic hybrid coatings for corrosion protection of building materials.[13] Combining PMMA with cerium oxide nanoparticles yielded excellent self-healing and anti-corrosion properties.

Coordination compounds of transition metals, such as niobium, tantalum and vanadium, have been popular in olefin polymerization research.[23–25] This is due to their ability to efficiently catalyze various mechanisms of polymer chain growth – often with high activity and control over stereochemistry. Early studies noted that vanadium-based catalysts are very effective in the polymerization of ethylene and its copolymerization with monomers containing polar groups.[26] However, their performance is limited by moderate thermal stability and catalyst time. Niobium and tantalum complexes – usually stabilized with triphenolate, alkoxy, amide or pyrazolyl ligands – also show high catalytic properties.[24,25,27] They can initiate the polymerization of olefins in a selective manner, enabling, for example, viable polymerization and efficient incorporation of comonomers. The high electrophilicity of group 5 metals is crucial, which makes it possible to precisely modify their catalytic properties through appropriate choice of ligands.

In this study, we explore how coordination environments of Nb(v), Ta(v), and V(iv) complexes impact the efficiency of polymerization and self-healing behavior, providing new insight into the rational design of adaptive materials. In the first step we synthesized novel crystalline Nb(v), Ta(v), and V(iv) coordination compounds with ligands such as 2-phenylpyridine, 4-phenylpyridine, and DMF, unlocking new catalytic potential for polymerization reactions. Secondly we applied these advanced catalysts to the production of polyethylene, ethylene/1-octene copolymers, and self-healing materials based on methyl methacrylate showcasing their versatility and efficiency in material synthesis. In the final step we investigated the self-healing behavior of materials based on methyl methacrylate, examining the impact of catalyst type, MMA con-

Table 1 Examples of self-healing polymers including properties

No.	Self-healing polymer	Details of self-healing process	Properties	Ref.
1	Diels–Alder polymers	Polymers utilizing Diels–Alder reactions for self-healing. DSC (differential scanning calorimetry) to study the reversibility of the reaction and thermal behavior	Reversible bonds at room temperature, thermoplasticity	7
2	Hydrogen-bonding polymers	Use dynamic hydrogen bonds for structural regeneration. FTIR (Fourier transform infrared spectroscopy) to analyze bond formation and dynamics	Flexibility, self-healing at room temperature	14
3	Disulfide bond polymers	Self-healing through reversible oxidation and reduction of disulfide bonds. UV-Vis spectroscopy for monitoring the oxidation/reduction process	Chemical stability, capability for multiple regenerations	15
4	Imine bond polymers	Polymers containing dynamic imine bonds. Tensile testing to assess mechanical properties and recovery after healing	Tensile strength, self-healing in the presence of moisture	16
5	Supramolecular polymers	Utilize non-covalent interactions for self-healing. NMR (nuclear magnetic resonance) for investigating dynamic interactions	High elasticity, reversible self-healing	17
6	Microcapsule-based polymers	Embedded microcapsules release healing agents upon damage. Scanning electron microscopy (SEM) to examine capsule release upon damage	Targeted self-healing, long-term durability	18
7	Shape memory polymers	Return to original shape upon heating, enabling self-healing. DMA (dynamic mechanical analysis) to study shape memory and recovery properties	Shape memory effect, thermal responsiveness	19
8	Ionic polymers	Incorporate ionic interactions for self-healing. Electrochemical impedance spectroscopy (EIS) for ionic conductivity and self-healing under electrical stimuli	High ionic conductivity, self-healing under electrical stimuli	20
9	Epoxy-based self-healing polymers	Epoxy resins modified for self-healing capabilities. Tensile testing and thermogravimetric analysis (TGA) to assess mechanical and thermal properties	High mechanical strength, thermal stability	21
10	Metal–ligand coordination polymers	Use metal–ligand interactions for dynamic self-healing. MALDI-TOF (matrix-assisted laser desorption/ionization time-of-flight mass spectrometry) to analyze metal–ligand interaction dynamics	Reversible coordination, robust mechanical properties	22

centration in the starting reaction mixture, and temperature on material recovery and processing, paving the way for next-generation, adaptive materials systems.

2. Results and discussion

2.1. Structures of Nb(v), Ta(v) and V(iv) complex compounds

The structures of the synthesized complex compounds are shown in Fig. 1 (CCDC numbers: 2391112, 2391113, and 2383525†). The Nb(v) complex crystallises in the triclinic $P\bar{1}$ space group. The $NbOCl_3$ molecule[28] is additionally coordinated by two dimethylformamide moieties in a *cis* mutual arrangement (Fig. S1a†).

In consequence, the Nb(v) cation adopts an octahedral coordination geometry. In the crystal structure the complex molecules are arranged in such a way that the organic fragments are grouped together as shown in Fig. S2a,† leading to a layer-like architecture. The crystal structure is stabilised mainly by numerous hydrogen-bond-like contacts between the oxygen or chlorine atoms and the adjacent aliphatic hydrogen atoms. The Ta(v) complex crystallizes as a multicomponent salt crystal in the triclinic $P\bar{1}$ space group. The asymmetric unit (ASU) (Fig. S1b†) contains an octahedral $TaCl_6^-$ and a chloride anion, two protonated 2-phenylpyridine moieties and a dichloromethane molecule. The crystal structure is characterise by a layered architecture. Organic fragments form layers parallel to the (012) crystal plane which are arranged alternately along the [001] direction with the anionic layers composed of Cl^-, $TaCl_6^-$ and solvent species (Fig. S2b†). In turn, when looking at the crystal packing along the Z axis, anions and cations create a chessboard pattern. The crystal structure is dominated by the electrostatic interactions between the charged species, however, some weaker $\pi\cdots\pi$ stacking contacts can also be detected (Fig. 1 and S1†). The Nb(v) and Ta(v) complexes crystallize in a ternary arrangement, in the same space group $P\bar{1}$, and their elemental cells each contain two structural units ($Z = 2$), indicating similarity in the crystal symmetry of the two compounds. Despite the identical space group, the differences in the size of the elemental cells are pronounced: for the Nb(v) complex, the volume is 655.8(3) $Å^3$, while for the Ta(v) complex it is as large as 1484.8(7) $Å^3$. Such a large difference is consistent with the fact that the tantalum complex has a much higher molecular weight (826.43 *vs.* 361.45 u) and a more extended structure, containing additional ions and molecules such as two cations $[C_{11}H_{10}N]^+$, an anion $[TaCl_6]^-$, a Cl^- ion and a solvent molecule CH_2Cl_2. Nevertheless, the calculated densities of the two complexes are very similar: 1.8304 g cm^{-3} for Nb(v) and 1.8486 g cm^{-3} for Ta(v), suggesting that the packing of molecules in the crystal is similar in both cases, regardless of the differences in mass and volume. The Nb–Cl bond lengths range from 2.365(2) to 2.404(3) Å, corresponding to typical lengths for Nb–Cl bonds in octahedral niobium(v) complexes, where they typically range between 2.3 and 2.5 Å. The small differences between these values suggest similar interaction strengths and similar symmetry around the niobium(v) cation. The Nb–O bond lengths, on the other hand, are more variable, ranging from 1.704(5) Å (for the Nb1–O3 bond) to 2.221(5) Å (for Nb1–O2). The shortest of these, 1.704 (5) Å, corresponds to the Nb=O bond, typical of high-oxidation transition metal oxides. The remaining, longer Nb–O bonds are of a coordination nature and are within the typical range for such bonds with O-donor ligands, such as ethers. The variation in the length of these bonds is indicative of the different electron influences of the ligands in the vicinity of the central metal atom.

The Ta(v) complex forms a multicomponent salt crystal with a layered structure where electrostatic interactions

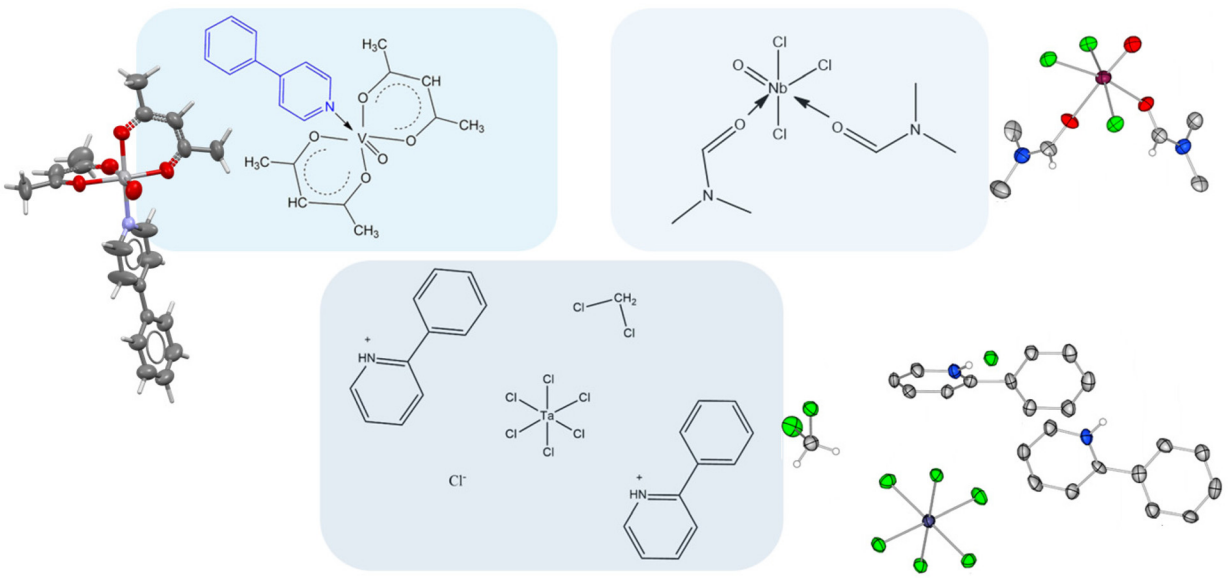

Fig. 1 Structures of synthesized V(iv), Nb(v) and Ta(v) complex compounds.

between charged species dominate, complemented by weaker π···π stacking contacts (Fig. 1 and S2†).

Our study revisits the VO(IV) complex first reported by Caira *et al.* (1972),[29] providing a detailed crystallographic analysis using single-crystal X-ray diffraction and first-principles modeling to address the missing structural details. The results confirm the monoclinic *C*2/*c* space group, highlight the influence of crystal packing on molecular geometry, and offer new insights into the structural flexibility and catalytic potential of vanadium-based compounds (Fig. 1, S3–S4 and Tables S1–S4†). The VO(IV) complex was originally reported in 1972 by Caira *et al.*[29] but the absence of fractional coordinates in the CCDC in the corresponding entry (CCDC number: 1237904) and lack of information in the corresponding article about the geometrical features of the phenylpyridyl ligand, vanadium coordination geometrical features (except vanadyl distance), disposition of acetylacetonate (acac) groups with respect vanadyl, crystal packing and intermolecular contacts, and, moreover, prompted us to further investigate its crystallographic features by single crystal X-ray diffraction and first principle modeling. $VO(acac)_2$(4-phenylpyridine) complex crystallizes in the monoclinic space group *C*2/*c*, with a single metal complex in the asymmetric unit (Fig. S3a†), confirming the presence of an unpaired electron in the complex. The unit cell parameters are as follows: a = 24.2547(1) Å, b = 8.0765(5) Å, c = 21.659(1) Å, β = 108.968(7)° (Table S2†). The unit cell volume of 4012.5(4) Å^3 suggests a closely packed structure, with 17.913 Å^3 per atom, indeed only a bit smaller than the value of 18 Å^3 per atom by the Kempster and Lipson rule.[30] Bond lengths between the central vanadium atom and its coordinating oxygen atoms (Table S3†) are consistent with those reported for similar complexes,[31] and very similar to the bond distances observed by Caira *et al.* for this same complex (when available).[29] In fact, some structural details of the V(IV)-based compound were initially reported by Caira *et al.* in 1972,[29] when the unit cell dimensions and the space group were correctly reported. In this paper, thanks to 1412 independent reflections, whose intensity was "estimated visually" (as stated by the authors) they solved the structure by Patterson methods, confirming the *cis* configuration of the quasi-octahedral vanadium complex, and also noting a not coplanar disposition of the vanadium with respect to the planar coordination system formed by N, O3, O4, and O5, according to the referenced paper's nomenclature. Such displacement was correctly estimated being 0.22(1) Å by the authors. These results are really impressive, given the instrumentations available in the early '70 of XX century and the large unit cell. However, two reasons suggested us to propose a new structural resolution. On one hand, the fractional atomic coordinates were not provided and are not available in the manuscript and in CSD. More importantly, in that article the structure is not discussed in detail. Angles and torsion angles are not given, and the structure could have some torsional conformations, especially involving the bipyridyl system. To further investigate conformational flexibility of the V(IV)-based complex, two molecular models with the geometric features reported in Table 2 were subjected to geometric optimization. The two experimental structures (model 1, from SC-XRD solved structure and model 2 inspired by Fig. S4† from Caira *et al.*), were used as input for the calculations. The main difference between the two models is the conformation of the phenyl pyridyl group and its orientation with respect to the vanadyl ligand, as evidenced by the torsion angles in Table S4.† Worth noting, after geometric optimization, both model 1 and model 2 converged to the same result, which is consistent with the one obtained experimentally in the present paper, except for the phenyl ring rotation with respect to the bipyridyl one. This suggests that the crystal packing imposes a molecular geometry (red complex in Fig. S4†) different from an energy minimum in the vacuum or in solution (blue complex in Fig. S4†). Therefore, it can be concluded that the vanadium-based compound, when acting as catalyst in solution without the constraints of crystal packing, assumes a conformation similar to that of the optimized model, with the vanadyl group well accessible from outside to complex.

The comparison with related structures is also noteworthy. The recently resolved structure of the $VO(acac)_2$ *N*-oxide complex (CCDC number: 2369265) adopts a *trans*-configuration, contrasting with the *cis*-configuration observed in the V-based complex. This structural difference can be attributed to the presence of an oxygen bridge between the nitrogen and vanadium atoms. In the vanadium complex, the direct bond between the nitrogen and vanadium atoms results in the bipyr-

Table 2 Results of ethylene homo- and copolymerization catalyzed by vanadium complex

Entry	Time (min)	Activator	1-Octene (mL)	Yield (g)	A [a]	1-Oct^{FTIR} [b] (%mol)	T_m [c] (°C)	X_C [c] (%)	M_w [d] (g mol^{-1})	M_w/M_n [d]
D-8-24	10	Et_2AlCl	—	3.43	68 600	—	135	65.8	263 400	2.22
D-9-24	10	Et_2AlCl	3	2.13	42 600	3.4	116	41.4	167 900	1.60
D-10-24	10	Et_2AlCl	1	3.11	62 200	2.4	123	47.0	230 300	3.32
D-11-24	10	Et_2AlCl	5	1.10	22 000	4.6	112	38.2	129 900	2.10
D-12-24	10	Et_2AlCl	2	2.19	43 800	2.9	118	42.7	138 800	1.89
D-13-24	6	$EtAlCl_2$	—	2.71	90 333	—	135	53.8	1 782 000	8.98
D-14-24	10	$EtAlCl_2$	3	2.01	40 200	7.9	108	30.9	294 200	2.35
D-16-24	10	$EtAlCl_2$	5	1.08	21 600	9.6	101	24.2	216 300	2.17

Polymerization conditions: vanadium complex 0.3 μmol, hexane 100 mL, ethylene 5 bar, Al/V (molar ratio) = 3000, ETA/V (molar ratio) = 200, temperature 60 °C. [a] Polymerization activity, kg mol_V^{-1} h^{-1}. [b] 1-Octene content in copolymer determined by FTIR method.[33] [c] Melting point and crystallinity determined by DSC. [d] Weight average molecular weight and polydispersity determined by HT-SEC using o-DCB as the mobile phase.

idine ligand being oriented almost perpendicularly to the V=O bond [∠N1···V1···O5 = 92.26°]. The slightly curved shape of the phenylpyridine terminus in the complex is peculiar, with an overall angle of approximately 8° between the two ends [∠N1···V1···C9 = 8.1(1)°]. Notably, it is surprising that almost half of this curvature occurs between the two aromatic rings, where only sp^2-hybridized atoms are present [∠C1···N1···C9 = 3.7(1)°]. In the *N*-oxide complex, the pyridine and phenyl rings are not coplanar, with a torsional angle of 26.90° between their planes. In contrast, the rings in the V(IV) complex are coplanar, although elevated atomic displacement parameters (ADPs) for atoms C15, C18, C20, and C21 suggest small rotational freedom around the N1···C1 axis. Finally, the $VO(acac)_2$ complex lacks efficient π–π stacking interactions (Fig. S3b†), which can be explained by the average distance between the stacked ring systems, which is incompatible with strong π–π interactions. This may be due to the absence of the oxygen bridge between nitrogen and vanadium and the particular configuration of the acetylacetonate chains (Fig. 2).

The UV-Vis diffuse reflectance spectrum of the $VO(acac)_2$ complex with 4-phenylpyridine shows two distinct absorption maxima: one at 443 nm and the other at 557 nm (Fig. S54†). The first can be attributed to LMCT-type transitions, *i.e.*, charge transfer from the ligand to the metal, while the second, weaker signal, corresponds to d–d-type transitions, which are typical of vanadium(IV) complexes. The presence of these bands confirms that vanadium is in the +4 oxidation state and suggests that the complex retains partial symmetry. For niobium(V) and tantalum(V) complexes, the situation is different – their spectra in the visible range are much less complex. The lack of clear signals above 350 nm indicates that d–d transitions do not occur, which is consistent with the electron configuration of d^0 for Nb(V) and Ta(V) (Fig. S54†). The weak band that appears between 200 and 350 nm can be attributed to LMCT transitions, *e.g.* from ligands such as Cl-. The absence of intense bands in the visible part of the spectrum indicates the simpler electron structure of niobium and tantalum complexes compared to that of vanadium.

2.2. Ethylene polymerization and ethylene/1-octene copolymerization

In the first step, the vanadium complex [$VO(acac)_2$(4-phenylpyridine)] was evaluated for ethylene polymerization and ethylene/1-octene copolymerization under specified conditions (0.3 μmol V, Al/V = 3000, ETA/V = 200, 60 °C). With Et_2AlCl as an activator, it showed high polymerization activity (68 600 kg mol^{-1}(V) h^{-1}). Addition of 1-octene comonomer reduced catalytic activity but enhanced comonomer incorporation (up to 22 000 kg mol^{-1}(V) h^{-1}) and 4.6 mol% for 0.3 mol dm^{-3} of 1-octene while lowering polymer melting points (135 °C to 112 °C) and crystallinity (65.8% to 38.2%). The molecular weight decreased with rising 1-octene content, indicating chain transfer to comonomer. Using $EtAlCl_2$ increased catalyst activity and enabled higher comonomer incorporation (7.9–9.6 mol%), producing copolymers with lower crystallinity and melting points (101–108 °C) (Table 2 and Fig. S9–S20†). Moreover, produced copolymers are characterized by narrow (M_w/M_n = 1.60–3.32) and monomodal molecular weight distribution, and they contain only isolated octene units between the ethylene blocks (Fig. S21, S54† and Fig. 3). The observed increase in catalytic activity compared to known V(IV) precatalysts can probably be attributed to enhanced intramolecular charge transfer, enhanced crystal field strength and increased electron density in the vicinity of the V(IV) ion, resulting from the presence of 4-phenylpyridine as a ligand. The formation of a coordination bond with this aromatic donor promotes efficient electron transfer from the d orbital to the π orbitals of the ligand, leading to favorable charge separation and lowering the energy of the donor levels.

Niobium(V) and tantalum(V) catalysts activated by Et_2AlCl or $EtAlCl_2$ exhibited low activity 58.5–708 kg mol^{-1}(V) h^{-1}. Et_2AlCl led to lower molecular weight polymers, while $EtAlCl_2$ produced ultra-high molecular weight polyethylene up to 1.6×10^6 g mol^{-1} (Table 3 and Fig. S22–S36†). Increasing Al/Nb(Ta) ratios boosted yield but reduced molecular weight, while lower reaction temperatures increased polymer molecular weight. Regardless of conditions, all synthesized polyethylenes were linear, with high melting temperatures (136–138 °C) and quite narrow molecular weight distributions (M_w/M_n = 2.13–3.99). Niobium(V)- and tantalum(V)-based catalysts had lower activity in copolymerization than in ethylene homopolymerization,

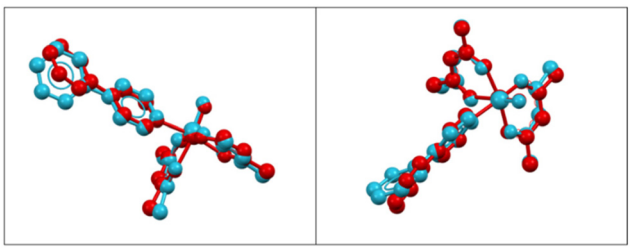

Fig. 2 SC-XRD model (red, model 1) and *in silico* geometrically optimized model (blue).

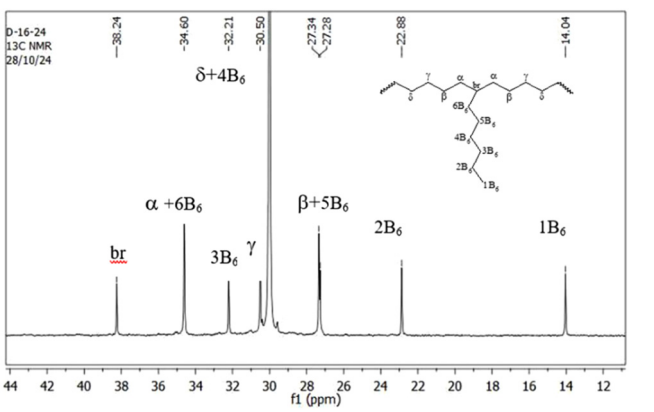

Fig. 3 $^{13}C\{^1H\}$ NMR spectrum of the copolymer produced by VO(acac)$_2$(4-phenylpiridyne)/$EtAlCl_2$ (D-16-24).

Table 3 Results of ethylene homo- and copolymerization catalyzed by niobium and tantalum catalysts

Entry	Cat.	Nb(Ta) (μmol)	Temp. (°C)	Activator	Al/Nb(Ta) (molar ratio)	ETA/Nb(Ta) (molar ratio)	Yield (g)	A [a]	1-Oct^{FTIR} [b] (%mol)	T_m [c] (°C)	X_C [c] (%)	M_w [d] (g mol^{-1})	M_w/M_n [d]
Nb-1	Niobium	0.5	60	Et_2AlCl	2000	200	0.118	708	—	138	61	678 000	2.70
Nb-2		1	60	Et_2AlCl	2000	200	0.122	366	—	136	61	548 800	3.07
Nb-3		1	60	$EtAlCl_2$	2000	200	0.043	129	—	136	49	1 599 800	3.12
Nb-4		1	60	Et_2AlCl	4000	200	0.179	537	—	138	63	416 500	2.75
Nb-5		1	40	Et_2AlCl	4000	200	0.150	450	—	138	59	704 400	2.16
Nb-6[e]		1	60	Et_2AlCl	4000	200	0.160	480	2.2	122	44	268 500	2.39
Nb-8[f]		1	60	Et_2AlCl	4000	200	0.023	69	2.8	119; 129	39	370 900	3.88
Ta-1	Tantalum	1	60	$EtAlCl_2$	2000	—	Traces	—	—	—	—	—	—
Ta-2		1	60	$EtAlCl_2$	2000	200	0.025	75	—	137	54	927 700	3.99
Ta-3		1	60	Et_2AlCl	2000	200	0.094	282	—	138	63	387 100	2.39
Ta-4		1	60	Et_2AlCl	4000	200	0.202	606	—	137	63	335 900	2.13
Ta-5[e]		1	60	Et_2AlCl	4000	200	0.050	150	2.6	123	42	184 300	2.01
Ta-6		0.5	30	Et_2AlCl	8000	400	0.060	360	—	138	56	363 200	2.75
Ta-7		2	60	Et_2AlCl	2000	200	0.039	58.5	—	137	60	1 032 100	2.19

Polymerization conditions: hexane 100 mL, time 20 min, ethylene 5 bar. [a] Polymerization activity, kg mol^{-1} h^{-1}. [b] 1-Octene content in copolymer determined by FTIR method.[33] [c] Melting point and crystallinity determined by DSC. [d] Weight average molecular weight and dispersity determined by HT-SEC. [e] 2 mL of 1-octene. [f] 3 mL of 1-octene in the feed.

incorporating 2.2–2.8 mol% of 1-octene. The resulting copolymers exhibited reduced melting points and crystallinities compared to polyethylene.

The conducted studies show that the type of activator used greatly influences the catalytic activity, and this effect depends on the central metal. In the case of the vanadium complex, the use of $EtAlCl_2$ activator results in higher catalytic activity (90 333 kg mol^{-1}(V) h^{-1}) than Et_2AlCl (68 600 kg mol^{-1}(V) h^{-1}). This may suggest that the more electrophilic nature of $EtAlCl_2$ promotes a more efficient activation mechanism. A different trend was observed for niobium and tantalum complexes – in their case, significantly higher catalytic activity is obtained with Et_2AlCl (708 and 606 kg mol^{-1}(V) h^{-1} respectively), while $EtAlCl_2$ yields much lower values (129 and 75 kg mol^{-1}(V) h^{-1}). This indicates that for Nb and Ta, the high electrophilicity of $EtAlCl_2$ may limit the efficiency of the formation of active catalytic centers or lead to their faster deactivation. The choice of activator therefore affects not only the initiation of the reaction itself, but also the stability and durability of the active center. Therefore, its optimization should be tailored to the specifics of a particular transition metal complex. Analyzing the catalytic activities of the Ta(v) complex, the compound described in this paper shows 35–24 times higher values of catalytic activity in ethylene polymerization than tantalum compounds with ligands such as tris(pyrazolyl)borate.[25] On the other hand, there are tantalum complex compounds with very high catalytic activities such as (η^5-C_5Me_4H)Ta(*N*-^{t}Bu)Me_2 which showed an activity of 1 206 000 kg mol^{-1}(V) atm^{-1} h^{-1}.[32]

The oxovanadium(IV) complex with 4-phenylpyridine described in this paper shows high catalytic activity in ethylene polymerization. Compared with the $VO(acac)_2$ complex, this is a 24-fold increase in catalytic activity in the polymerization of ethylene, which confirms the significant effect of 4-phenylpyridine on the catalytic properties of the complex.[34] In the case of vanadium(IV) salen complexes, this shows about 9-fold lower catalytic activity.[35] The oxovanadium(IV) complex compound with 4-phenylpyridine has about 2 times higher catalytic activity than the cyclopentadienyl vanadium(IV) complex.[36] In the case of vanadium(IV) complexes with cyclohexyl groups, these show about 5 times lower catalytic activity compared to the complex of oxovanadium(IV) with 4-phenylpyridine. With the activator in this case being $Et_3Al_2Cl_3$.[36] In the case of tantalum complex compounds with tris(pyrazolyl)borate ligands, their catalytic activity in ethylene polymerization is 24 to 35 times lower than that of the tantalum compound described in this report.[25] On the other hand, there are also tantalum compounds that show very high catalytic activities such as (η^5-C_5Me_4H)Ta(*N*-*t*Bu)Me_2 which has an activity in ethylene polymerization equal to 1 206 000 g mol atm^{-1} h^{-1}.[32] Comparing the niobium(v) complex compound described in our work with others known in the literature, it can be seen that it shows 8–15 times higher catalytic activities than, for example, di- and triphenolate complexes of Nb(v).[24,27]

2.3. Fabrication and material properties of self-healing materials based on methyl methacrylate

MMA represents an interesting raw material for the synthesis of self-healing materials in the construction industry, due to its ability to rapidly polymerize, as well as its favourable mechanical properties. Furthermore, its low viscosity allows it to effectively penetrate micro-cracks, which promotes the autonomous structural regeneration of these materials. The results of conducted syntheses and products characterization are summarized in Fig. 4, Table S5 (detailed results) and Fig. S37–S53.†

These findings highlight significant trends in catalytic performance, thermal properties, and molecular weight distribution, reflecting the effects of catalyst type. The activity of the catalysts, varies significantly across the entries. For V(IV), the T_g peaks at 30 °C for V-PE-30MMA. The T_g decreases to 33 °C for sample V-PE-50MMA, highlighting increased phase separation. In contrast, the copolymerization products obtained using Nb

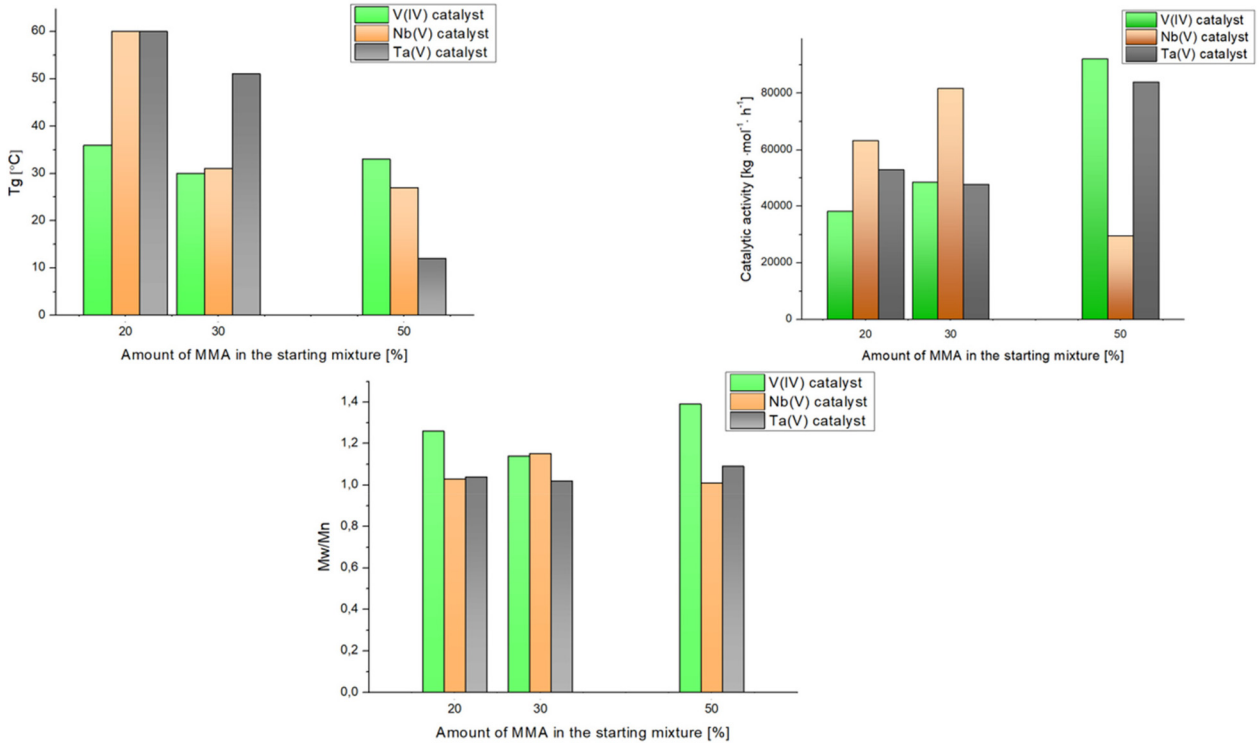

Fig. 4 The relationship between the amount of MMA and T_g, M_w/M_n, and catalytic activity.

(v)- and Ta(v)-based catalysts show less consistent trends, with T_g values decreasing significantly particularly for Ta-PE-50MMA (12 °C), indicative of greater disruption of the self-healing matrix.

The molecular weight distribution (M_w/M_n), indicative of material uniformity, ranges from 1.01 to 1.39 across all entries. The samples synthesized with V(IV)-based catalysts exhibit broader distributions (*e.g.*, 1.39 for V-PE-50MMA), reflecting increased chain irregularities. Conversely, Nb(v)- and Ta(v)-based systems display narrower distributions (1.01–1.15), suggesting more controlled polymerization. This difference might stem from varying propagation and termination mechanisms influenced by the catalyst's electronic and steric properties. Vanadium-based catalyst demonstrates the highest activity and widest range of thermal and structural properties, making it the most versatile for tailoring copolymer properties.

2.4. Rheology and morphology studies of self-healing materials based on methyl methacrylate

The viscosity curves and flow curves provide insight into the rheological behavior of the samples at 60 and 70 °C (Fig. 5). These results highlight the influence of amount of MMA used for the process on the viscosity and flow properties of the copolymers under varying shear rates. At both 60 and 70 °C, the viscosity of the samples decreases with increasing shear rate, demonstrating shear-thinning behavior typical of non-Newtonian fluids. The sample V-PE-50MMA exhibits the highest viscosity across all shear rates, followed by the V-PE-30MMA and V-PE-20MMA samples. This trend indicates that higher MMA content increases the molecular interactions and entanglements within the polymer matrix, leading to greater resistance to flow. The temperature effect is also evident, with viscosity values at 70 °C being lower than those at 60 °C for all copolymers. This reduction in viscosity with increasing temperature is expected due to the enhanced molecular mobility and reduced intermolecular forces at elevated temperatures. The difference in viscosity between the copolymers becomes more pronounced at higher shear rates, suggesting that the influence of amount of MMA used for the process is more significant under dynamic flow conditions. The flow curves further confirm the shear-thinning behavior of the samples, as the shear stress increases non-linearly with shear rate. At both temperatures, the V-PE-50MMA demonstrates the highest shear stress at a given shear rate, followed by the V-PE-30MMA and V-PE-20MMA. This behavior is consistent with the viscosity data, as higher amount of MMA used for the process leads to increased resistance to deformation under applied stress. The effect of temperature is again evident, with lower shear stress values observed at 70 °C compared to 60 °C for all copolymers. This indicates that the polymer chains are more easily deformed at higher temperatures, reducing the overall resistance to flow. Additionally, the linearity of the flow curves at higher shear rates suggests that the copolymers approach a pseudo-Newtonian flow regime under these conditions. At higher shear rates, all analyzed

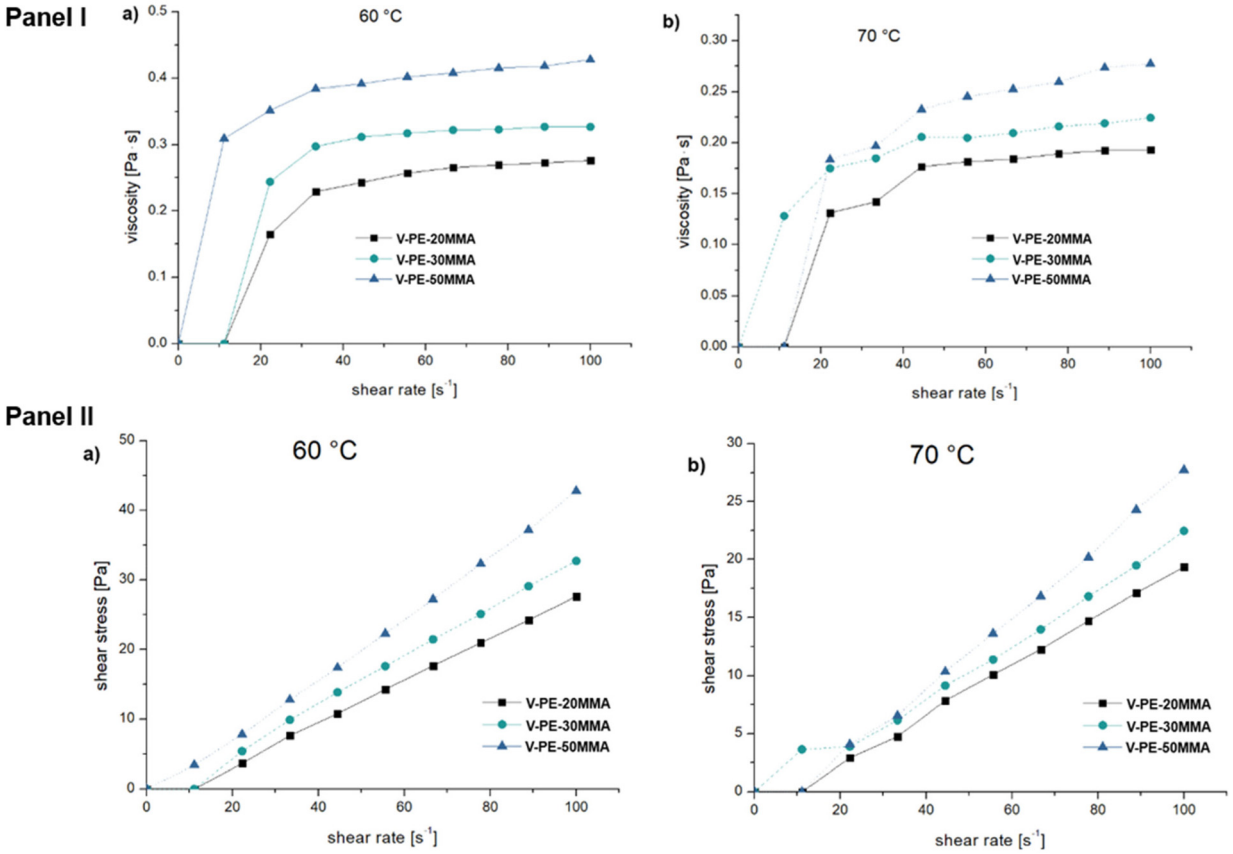

Fig. 5 Panel I: Viscosity curves of the V-PE-20MMA, V-PE-30MMA and V-PE-50MMA at (a) 60 °C, (b) 70 °C. Panel II: Flow curves of the V-PE-20MMA, V-PE-30MMA and V-PE-50MMA at (a) 60 °C, (b) 70 °C.

samples showed a tendency to stabilize viscosity, suggesting a shift to a pseudo-Newtonian flow regime. This behavior may be related to the molecular structure of the copolymers – higher MMA content promotes the formation of cross-links and limits the mobility of chain segments, which in turn affects the way the material reorganizes under shear stress.

The observed trends in both viscosity and flow behavior can be attributed to the structural and compositional differences between the products. Higher amount of MMA used for the process likely results in increased rigidity and molecular weight, contributing to the higher viscosity and shear stress values. The enhanced intermolecular interactions, such as hydrogen bonding or dipole–dipole interactions, may also play a role in the increased resistance to flow. The rheological results shown in Fig. 5 show that increasing the MMA content of V-PE-MMA materials results in higher viscosity and shear stress at the analyzed shear rates. This means that the internal structure of the material becomes a more compact network that better resists deformation. Particularly clear effects of this phenomenon can be seen in the V-PE-50MMA sample, where stronger shear responses were observed. This may indicate changes in the linear range of viscoelasticity and a shift in yield stress as the proportion of MMA increases. The collected data clearly show that the concentration of MMA has a significant effect on the viscoelastic properties of the analyzed materials.

The rheological analysis reveals that the samples exhibit pronounced shear-thinning behavior, characteristic of non-Newtonian fluids, with both viscosity and shear stress being markedly dependent on the amount of MMA used for the process and temperature. An increase in amount of MMA used for the process results in elevated viscosity and shear stress values, attributed to enhanced intermolecular interactions and greater molecular chain entanglement. Conversely, higher temperatures lead to a reduction in these parameters, driven by increased molecular mobility and a consequent decrease in resistance to flow. These findings offer critical insights into the rheological properties of the copolymers, underscoring their significance in tailoring processing conditions and optimizing their performance in self-healing polymer applications.

The SEM images reveal the morphology of MMA-based materials synthesized using a V(IV) complex as a catalyst, with varying amounts of MMA used in the process (20 vol%, 30 vol%, and 50 vol%) (Fig. 6). These images highlight the structural changes in the copolymers as the MMA proportion increases, providing insights into the relationship between composition and morphology. For V-PE-20MMA, the SEM image at 100-fold magnification shows a block-like structure

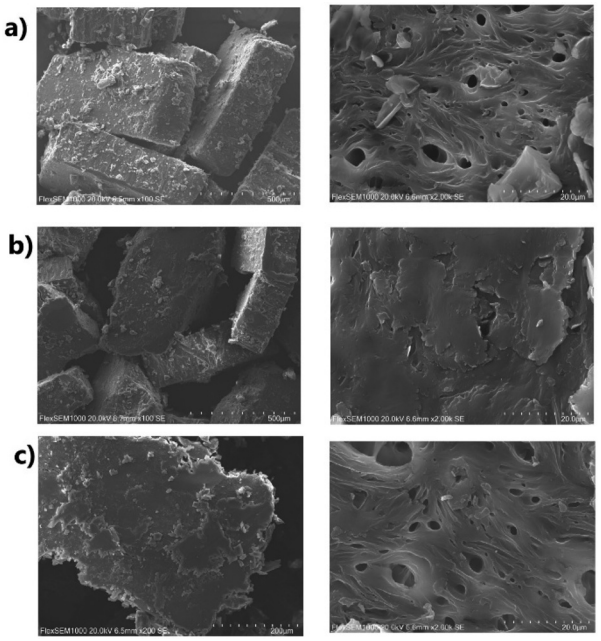

Fig. 6 SEM images for (a) V-PE-20MMA-100-fold magnification on the right, 2000-fold magnification on the left; (b) V-PE-20MMA-100-fold magnification on the right, 2000-fold magnification on the left; (c) V-PE-20MMA-200-fold magnification on the right, 2000-fold magnification on the left.

characterized by relatively smooth surfaces and sharp edges. The blocks appear compact and well-defined, with minimal porosity or surface irregularities. At 2000-fold magnification, the surface displays a network of small pores (20–78 μm) and cavities, suggesting a moderate degree of porosity. The irregularly shaped pores and moderately rough surface texture indicate partial phase separation or incomplete mixing during the polymerization process. For the V-PE-30MMA the morphology exhibits a more fragmented appearance compared to the V-PE-20MMA sample. At 100-fold magnification, the block-like structures become smaller and less uniform, with rougher surfaces and visible cracks. At 2000-fold magnification, the surface texture appears rougher, featuring a denser network of pores and voids. These pores are larger and more interconnected, reflecting increased heterogeneity in the copolymer structure as the MMA proportion rises. At V-PE-50MMA, the morphology becomes even more irregular and less compact. At 100-fold magnification, the copolymer consists of larger, loosely aggregated fragments with highly uneven surfaces and significant roughness. At 2000-fold magnification, the surface is dominated by a highly porous network with large, irregularly shaped pores. The pronounced porosity suggests that the higher amount of MMA used for the process leads to greater phase separation and structural heterogeneity. The samples morphology evolves from compact and block-like at lower MMA proportions to more fragmented and porous structures as the MMA proportion increases. The increasing porosity and surface roughness with higher quantity of MMA utilized in the process indicate reduced compatibility between ethylene and MMA during copolymerization. This trend is likely due to differences in their chemical properties and their interaction with the V(IV) catalyst.

The structure of these complexes strongly affects the polymerization process and the final morphology of the copolymers. Oxovanadium(IV) complexes with acetylacetonate and 4-phenylpyridine have a stable coordination geometry. This helps control polymer chain growth and forms tighter networks, especially at lower MMA content. Niobium complexes, due to chloride ions and DMF, create more varied active sites. This leads to more irregular copolymer morphology, seen in SEM as higher porosity and finer structures at higher MMA levels. The tantalum(V) complex shows strong ionic interactions as a multicomponent salt. This creates a more ionic and branched network. It can increase copolymer stiffness, viscosity, and shear stress during rheology tests. The rheological and morphological changes (Fig. 5 and 6) match these structural differences in the catalytic complexes. Higher MMA amounts, combined with complex geometry, raise chain entanglement and intermolecular forces. This results in higher viscosity, stiffness, and resistance to deformation.

2.5. Studies of self-healing properties

The mechanism of self-repair is based on the dynamic nature of hydrogen bonds, which allow intermolecular networks to reform when the structure is broken. In the case of self-healing materials based on methyl methacrylate, which contain functional groups capable of forming hydrogen bonds, this process occurs due to interactions between hydroxyl groups, and dynamic transformation of hydrogen bonds under temperature and mechanical stress. In self-healing materials based on methyl methacrylate, hydrogen bonds can form primarily between the polar groups. The temperature can impact the strength and number of hydrogen bonds, as higher temperatures may increase the mobility of the molecules, promoting easier healing through these non-covalent interaction. The self-healing properties of self-healing materials based on methyl methacrylate were systematically evaluated under different conditions on the recovery process (Fig. 7 and 8). There is no carbonyl group band in the FTIR spectra (including the ATR method) of all self-healing materials. There is also no C═O carbon atom signal in the ^{13}C NMR spectra (Fig. 7, 8 and S46–53†). It is most likely that the synthesis of self-healing materials results in the formation of the enolic form C–O instead of C═O.[37] In the FTIR spectrum (ATR method) of polyMMA, the carbonyl group band is at 1728 cm^{-1}. Therefore, both comonomers must be present for such a product to be formed. The high melting point may indicate polyalcohol and hydrogen bond type interactions. At 25 °C, the healing time decreases significantly as the amount of MMA used during the synthesis process increases. For the V(IV)-catalyzed samples, the healing time reduces from 4.5 hours in the sample obtained with the smallest amount of MMA used for the synthesis to 35 minutes in the sample prepared with the largest amount. A similar trend is observed for Nb(V)- and Ta(V)-cata-

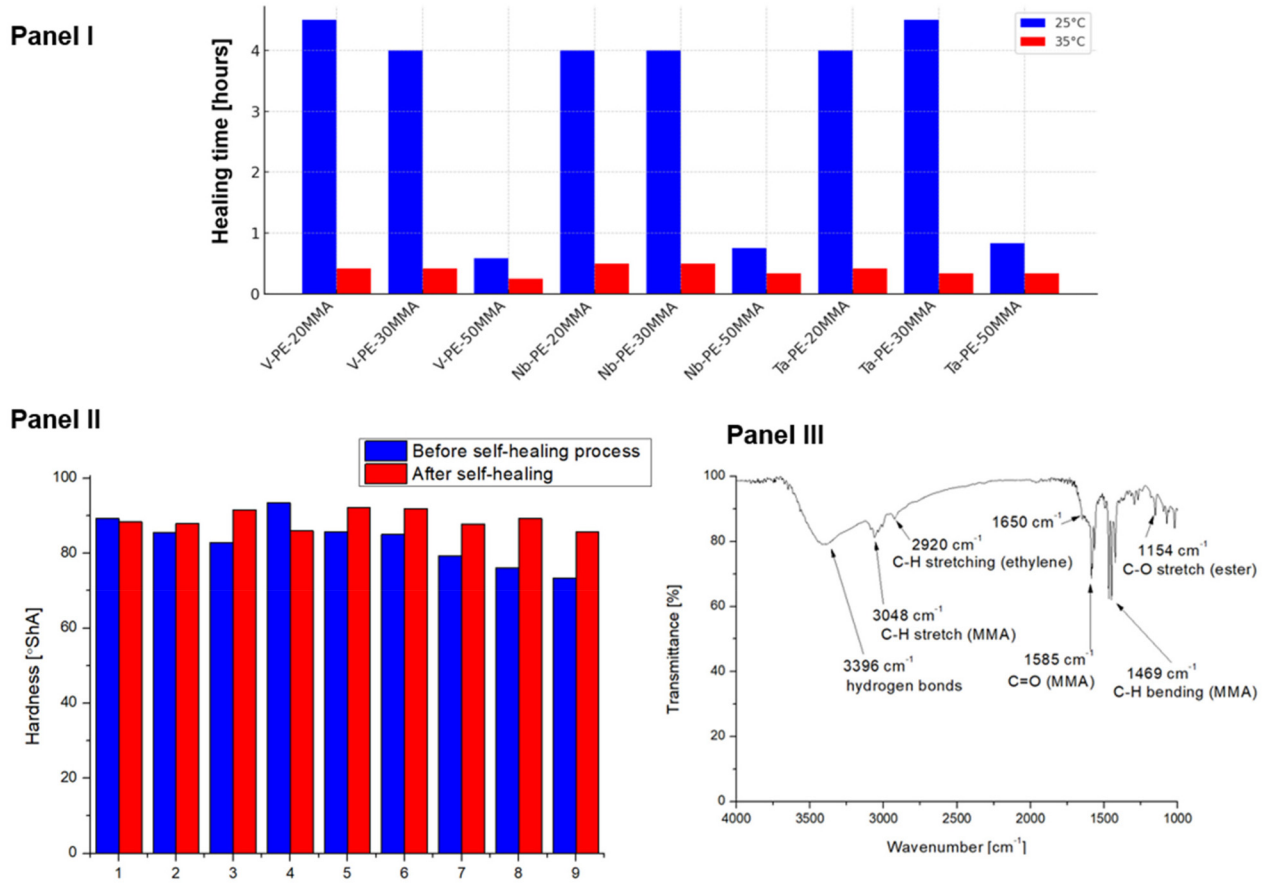

Fig. 7 Panel I: Dependence of self-healing time on temperature and sample type. The time measured until the gap between the material surfaces was no longer visible to the naked eye, and after lifting, the material formed a single, cohesive piece without breaking apart. Panel II: Hardness properties of materials based on methyl methacrylate. Sample 1 denotes V-PE-20MMA, sample 2 = V-PE-30MMA, sample 3 = V-PE-50MMA, sample 4 = Nb-PE-20MMA, sample 5 = Nb-PE-30MMA, sample 6 = Nb-PE-50MMA, sample 7 = Ta-PE-20MMA, sample 8 = Ta-PE-30MMA, sample 9 = Ta-PE-50MMA. Panel III: FTIR spectrum of Nb-PE-30MMA after self-healing process.

lyzed materials. For instance, the healing time decreases from 4 hours in the Nb(v)-catalyzed sample synthesized with the smallest MMA input to 45 minutes in the sample obtained with the largest MMA input. These results suggest that using a greater amount of MMA during the synthesis improves the healing efficiency at room temperature, likely due to increased compatibility within the polymeric matrix. At 35 °C, the trend remains consistent, with samples obtained using a greater amount of MMA exhibiting shorter healing times. The V(IV)-catalyzed material synthesized with the largest %vol. of MMA achieves the shortest healing time (15 minutes), followed by the Nb(v)- and Ta(v)-catalyzed materials, which both heal in 20 minutes. The reduction in healing time at elevated temperatures suggests enhanced mobility of polymer chains and better diffusion at the healing interface, particularly in materials prepared with a larger input of MMA. The choice of catalyst also plays a critical role in determining the healing efficiency. Across all levels of MMA used, the V(IV)-catalyzed samples exhibit the shortest healing times, both at 25 °C and 35 °C. For example, at 25 °C, the V(IV)-catalyzed material synthesized with the largest MMA input heals in 35 minutes, compared to 45 minutes and 50 minutes for the Nb(v)- and Ta(v)-based equivalents, respectively. At 35 °C, the V(IV)-catalyzed material maintains its advantage with a healing time of 15 minutes, highlighting the superior catalytic efficiency of the V(IV) system in facilitating polymer chain dynamics during the self-healing process. Nb(v)- and Ta(v)-catalyzed samples exhibit similar healing behaviors, with slightly longer times compared to V(IV). However, these systems also show a consistent decrease in healing time with increasing amounts of MMA used during synthesis, reflecting their suitability for self-healing applications, albeit with slightly reduced efficiency. The data reveals a clear improvement in healing efficiency with increased temperature across all catalyst systems and amounts of MMA used. At 35 °C, the healing times are substantially shorter than at 25 °C, indicating that the self-healing process is thermally activated. The enhanced chain mobility and faster diffusion at elevated temperatures facilitate quicker recovery of the material's mechanical integrity. Time-resolved FTIR spectra (Fig. S55†) collected during the first 6 minutes of the self-healing process show dynamic changes in the absorption bands, particularly at 3428 cm^{-1} (hydrogen bonding),

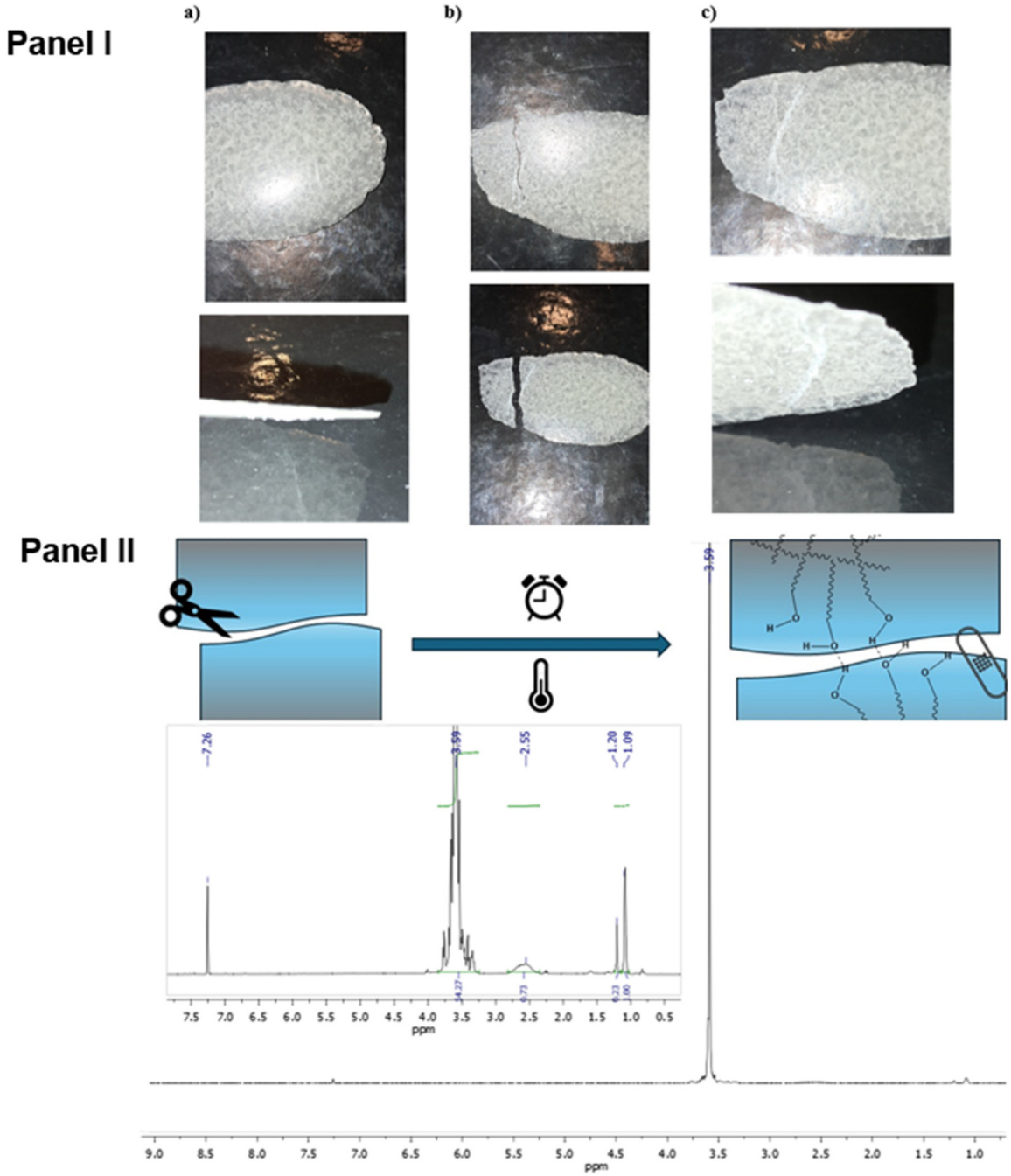

Fig. 8 Panel I: Example images of Nb-PE-30MMA. (a) Original sample (obtained after melting in a mold); (b) sample after cutting (damage of a 3 mm thick material); (c) sample after the self-healing process at 35 °C. Panel II: A diagram of the self-healing process in materials based on methyl methacrylate. ^{1}H and ^{13}C NMR for materials obtained using V(IV)-catalyst.

2888 cm^{-1} (C–H stretching), 1967 cm^{-1} and 1596 cm^{-1} (associated with conjugated systems or carbonyl groups). The progressive decrease in intensity of the hydroxyl-related band suggests reorganization and reformation of intermolecular interactions, confirming the molecular basis of the observed macroscopic healing.

These findings suggest that samples with higher MMA input are particularly well-suited for applications requiring rapid self-healing under mild conditions. The tunable healing properties, dictated by composition and environmental factors, could make these materials viable for coatings, protective films, or functional components in soft robotics or lightweight structures. Additionally, the robust performance at slightly elevated temperatures indicates potential for use in systems exposed to moderate thermal fluctuations. The hardness values of the polymer samples before and after the self-

healing process, measured using a Shore A Durometer, reveal the influence of the self-healing process and the varying concentrations of MMA (methyl methacrylate) introduced into the reaction system (20 vol%, 30 vol%, and 50 vol%) on the mechanical properties of the samples (Fig. 7). The results show that for the V-PE samples, the hardness decreased slightly after the self-healing process at 20 vol% MMA, from 89.2 ± 0.7 to 88.5 ± 1.7, suggesting a minor loss in mechanical integrity. However, with higher MMA content, the hardness increased. Specifically, for 30 vol% MMA, the hardness rose from 85.6 ± 0.5 to 88.0 ± 0.9, and for 50 vol% MMA, it increased significantly from 82.9 ± 1.1 to 91.6 ± 1.2. This indicates that higher MMA concentrations applied to the process improve the self-healing efficiency by enhancing the formation of hydrogen bonds or other interactions that aid in the recovery of the material. In the case of the Nb-PE samples, the hardness showed a more pronounced variation. At 20 vol% MMA, there was a noticeable decrease in hardness from 93.4 ± 0.3 to 86.0 ± 0.5, likely due to incomplete recovery of the polymer network. However, for 30 vol% MMA, the hardness increased significantly from 85.8 ± 0.7 to 92.1 ± 0.3, and at 50 vol% MMA, it rose from 85.1 ± 0.8 to 91.9 ± 0.8. This suggests that the self-healing process was more efficient in these samples, likely due to the formation of more stable hydrogen bonds at higher MMA vol% in the reagents mixture. For the Ta-PE samples, the hardness increased in all cases after the self-healing process. At 20 vol% MMA, the hardness rose from 79.3 ± 1.2 to 87.8 ± 0.9, at 30 vol% MMA from 76.1 ± 0.7 to 89.2 ± 1.3, and at 50 vol% MMA from 73.3 ± 1.0 to 85.7 ± 1.2. These results indicate that the Ta-PE matrix responds well to the self-healing process, with higher MMA concentrations in the reaction mixture contributing to more effective recovery.

Other examples of self-healing materials obtained using ethylene or MMA have been described in the literature. The self-healing behavior of ethylene and MMA-based copolymers aligns with previous studies on various polymer systems utilizing different healing mechanisms. Ionic crosslinks in EMAA ionomers,[38] dynamic supramolecular motifs in EBA copolymers,[39] and thermally reversible Diels–Alder reactions in EVA copolymers have all demonstrated effective recovery of mechanical properties after thermal activation.[40] Additionally, microencapsulated healing agents in ethylene-co-methyl acrylate and ionic interactions in ethylene/norbornene copolymers facilitate autonomous repair. The findings indicate that higher MMA content enhances self-healing efficiency, particularly at elevated temperatures, consistent with trends observed in other copolymers utilizing dynamic interactions, crosslinking, or encapsulated healing mechanisms.[41]

3. Conclusions

In summary, the study confirmed that the coordination geometry and type of central metal of Nb(v), Ta(v) and V(iv) have a significant impact on the structure, properties and functionality of polymeric materials. Although the Nb(v) and Ta(v) complexes belong to the same spatial group, they form completely different crystal structures – the Nb complex is characterised by a compact form stabilised by hydrogen interactions, while Ta builds a layered structure where electrostatic forces and π···π stacking dominate. An interesting aspect is the presence of an Nb=O bond, typical of highly oxidised oxide complexes. On the other hand, V(iv) complexes, such as [$VO(acac)_2$(4-phenylpyridine)], stood out for having the highest catalytic activity in ethylene polymerisation and copolymerisation with 1-octene, as well as the shortest regeneration time in self-repairing materials.

The use of these complexes as catalysts allowed precise control of the mechanical and thermal properties of the resulting materials. V(iv) complexes not only increase the efficiency of the polymerisation process, but also support the ability of the materials to self-heal, especially under conditions of increased MMA concentration and elevated temperature. In comparison, Nb(v) and Ta(v) complexes showed lower activity and lower copolymerisation efficiency. The results clearly demonstrate the potential of Nb(v), Ta(v) and V(iv) complexes in the creation of advanced and adaptive materials for modern technological applications.

Author contributions

Joanna Drzeżdżon: conceptualization, validation, project administration, investigation, methodology, data curation, writing – original draft, funding acquisition. Marzena Białek: investigation, writing – original draft. Stefania Zappia: investigation, writing – original draft. Mattia Lopresti: investigation, writing – original draft. Luca Palin: investigation, writing – original draft. Katarzyna N. Jarzembska: investigation, writing – original draft. Radosław Kamiński: investigation, writing – original draft. Janusz Datta: resources, writing – review & editing.

Data availability

The data supporting this article have been included as part of the ESI.†

Conflicts of interest

There are no conflicts to declare.

Acknowledgements

This research was supported by UGrants-start program (Poland) under grant no. 533-T000-GS38-24. The authors would like to thank Prof. Marco Milanesio for his assistance. The authors also wish to thank Mr Daniele Piovani for the acquisition of the SEC chromatograms. The in-house X-ray diffraction experiments were carried out at the Department of

Physics, University of Warsaw, on a Rigaku Oxford Diffraction SuperNova diffractometer, which was co-financed by the European Union within the European Regional Development Fund (POIG.02.01.00-14-122/09). The authors wish to thank Dr Eng. Krzysztof Formela and MSc Eng. Agata Rodak for their assistance in capturing the SEM images.

References

1 T. Speck, G. Bauer, F. Flues, K. Oelker, M. Rampf, A. C. Schüssele, M. von Tapavicza, J. Bertling, R. Luchsinger, A. Nellesen, A. M. Schmidt, R. Mülhaupt and O. Speck, in *Materials Design Inspired by Nature: Function Through Inner Architecture*, ed. P. Fratzl, J. Dunlop and R. Weinkamer, The Royal Society of Chemistry, 2013, pp. 359–389.
2 R. S. Trask, H. R. Williams and I. P. Bond, *Bioinspiration Biomimetics*, 2007, **2**, P1–P9.
3 K. Van Tittelboom, K. Adesanya, P. Dubruel, P. Van Puyvelde and N. De Belie, *Smart Mater. Struct.*, 2011, **20**, 125016.
4 S. Utrera-Barrios, R. Verdejo, M. A. López-Manchado and M. Hernández Santana, *Mater. Horiz.*, 2020, **7**, 2882–2902.
5 L. Zhang, Z. Liu, X. Wu, Q. Guan, S. Chen, L. Sun, Y. Guo, S. Wang, J. Song, E. M. Jeffries, C. He, F. L. Qing, X. Bao and Z. You, *Adv. Mater.*, 2019, **31**, 1901402.
6 Y. Yang and M. W. Urban, *Adv. Mater. Interfaces*, 2018, **5**, 1800384.
7 K. S. Toohey, N. R. Sottos, J. A. Lewis, J. S. Moore and S. R. White, *Nat. Mater.*, 2007, **6**, 581–585.
8 S. Burattini, H. M. Colquhoun, J. D. Fox, D. Friedmann, B. W. Greenland, P. J. F. Harris, W. Hayes, M. E. MacKay and S. J. Rowan, *Chem. Commun.*, 2009, **44**, 6717–6719.
9 E. Krieg, M. M. C. Bastings, P. Besenius and B. Rybtchinski, *Chem. Rev.*, 2016, **116**, 2414–2477.
10 C. H. Li and J. L. Zuo, *Adv. Mater.*, 2020, **32**, 1903762.
11 M. Araújo, S. Chatrabhuti, S. Gurdebeke, N. Alderete, K. Van Tittelboom, J. M. Raquez, V. Cnudde, S. Van Vlierberghe, N. De Belie and E. Gruyaert, *Cem. Concr. Compos.*, 2018, **89**, 260–271.
12 S. Taheri and S. M. Clark, *Int. J. Concr. Struct. Mater.*, 2021, **18**, 8.
13 S. V. Harb, A. Trentin, T. A. C. de Souza, M. Magnani, S. H. Pulcinelli, C. V. Santilli and P. Hammer, *Chem. Eng. J.*, 2020, **383**, 123219.
14 P. Cordier, F. Tournilhac, C. Soulié-Ziakovic and L. Leibler, *Nature*, 2008, **451**, 977–980.
15 H. P. Xiang, M. Z. Rong and M. Q. Zhang, *ACS Sustainable Chem. Eng.*, 2016, **4**, 2715–2724.
16 Y. Chen, A. M. Kushner, G. A. Williams and Z. Guan, *Nat. Chem.*, 2012, **4**, 467–472.
17 M. Burnworth, L. Tang, J. R. Kumpfer, A. J. Duncan, F. L. Beyer, G. L. Fiore, S. J. Rowan and C. Weder, *Nature*, 2011, **472**, 334–337.
18 S. R. White, N. R. Sottos, P. H. Geubelle, J. S. Moore, M. R. Kessler, S. R. Sriram, E. N. Brown and S. Viswanathan, *Nature*, 2001, **409**, 794–797.
19 D. Habault, H. Zhang and Y. Zhao, *Chem. Soc. Rev.*, 2013, **42**, 7244–7256.
20 S. Y. Zheng, S. Mao, J. Yuan, S. Wang, X. He, X. Zhang, C. Du, D. Zhang, Z. L. Wu and J. Yang, *Chem. Mater.*, 2021, **33**, 8418–8429.
21 D. Y. Wu, S. Meure and D. Solomon, *Prog. Polym. Sci.*, 2008, **33**, 479–522.
22 S. J. Rowan, S. J. Cantrill, G. R. L. Cousins, J. K. M. Sanders and J. F. Stoddart, *Angew. Chem., Int. Ed.*, 2002, **41**, 898–952.
23 K. Nomura and S. Zhang, *Chem. Rev.*, 2011, **111**, 2342–2362.
24 C. Redshaw, D. M. Homden, M. A. Rowan and M. R. J. Elsegood, *Inorg. Chim. Acta*, 2005, **358**, 4067–4074.
25 K. Michiue, T. Oshiki, K. Takai, M. Mitani and T. Fujita, *Organometallics*, 2009, **28**, 6450–6457.
26 W. L. Carrick, R. W. Kluiber, E. F. Bonner, L. H. Wartman, F. M. Rugg and J. J. Smith, *J. Am. Chem. Soc.*, 1960, **82**, 3883–3887.
27 A. M. Raspolli Galletti and G. Pampaloni, *Coord. Chem. Rev.*, 2010, **254**, 525–536.
28 D. E. Sands, A. Zalkin and R. E. Elson, *Acta Crystallogr.*, 1959, **12**, 1–6.
29 M. R. Caira, J. M. Haigh and L. R. Nassimbeni, *Inorg. Nucl. Chem. Lett.*, 1972, **8**, 109–112.
30 C. J. E. Kempster and H. Lipson, *Acta Crystallogr., Sect. B*, 1972, **28**, 3674.
31 O. A. O. Alshammari, S. Maisara, B. Alshammari, M. R. Alshammari, V. Rakic, J. Dimitrić Marković, V. Jevtovic and D. Dimić, *Molecules*, 2024, **29**, 1213.
32 S. Feng, G. R. Roof and E. Y. X. Chen, *Organometallics*, 2002, **21**, 832–839.
33 M. SudoŁ, K. Czaja and M. BiaŁek, *Polymers*, 2000, **45**, 405–410.
34 L. A. Rishina, Y. V. Kissin, S. S. Lalayan, P. M. Nedorezova and V. G. Krasheninnikov, *Polym. Int.*, 2022, **71**, 338–347.
35 M. Białek and K. Czaja, *J. Polym. Sci., Part A: Polym. Chem.*, 2008, **46**, 6940–6949.
36 H. Hagen, J. Boersma and G. Van Koten, *Chem. Soc. Rev.*, 2002, **31**, 357–364.
37 M. M. Marques, S. Fernandes, S. G. Correia, S. Caroço, P. T. Gomes, A. R. Dias, J. Mano, M. D. Rausch and J. C. W. Chien, *Polym. Int.*, 2001, **50**, 579–587.
38 R. J. Varley and S. van der Zwaag, *Acta Mater.*, 2008, **56**, 5737–5750.
39 N. Kuhl, S. Bode, M. D. Hager and U. S. Schubert, in *Self-Healing Materials, Advances in Polymer Science*, ed. M. D. Hager, S. van der Zwaag and U. S. Schubert, Springer, Cham, Switzerland, 2016, vol. 273, p. 1.
40 X. Chen, M. A. Dam, K. Ono, A. Mal, H. Shen, S. R. Nutt, K. Sheran and F. Wudl, *Science*, 2002, **295**, 1698–1702.
41 B. J. Blaiszik, N. R. Sottos and S. R. White, *Compos. Sci. Technol.*, 2008, **68**, 978–986.